LETTER

https://doi.org/10.1038/s41586-018-0680-3

Cryo-EM structures of a human ABCG2 mutant trapped in ATP-bound and substrate-bound states

Ioannis Manolaridis[1,4], Scott M. Jackson[1,4], Nicholas M. I. Taylor[2,3,4], Julia Kowal[1,4], Henning Stahlberg[2]* & Kaspar P. Locher[1]*

ABCG2 is a transporter protein of the ATP-binding-cassette (ABC) family that is expressed in the plasma membrane in cells of various tissues and tissue barriers, including the blood–brain, blood–testis and maternal–fetal barriers[1–4]. Powered by ATP, it translocates endogenous substrates, affects the pharmacokinetics of many drugs and protects against a wide array of xenobiotics, including anti-cancer drugs[5–12]. Previous studies have revealed the architecture of ABCG2 and the structural basis of its inhibition by small molecules and antibodies[13,14]. However, the mechanisms of substrate recognition and ATP-driven transport are unknown. Here we present high-resolution cryo-electron microscopy (cryo-EM) structures of human ABCG2 in a substrate-bound pre-translocation state and an ATP-bound post-translocation state. For both structures, we used a mutant containing a glutamine replacing the catalytic glutamate ($ABCG2_{EQ}$), which resulted in reduced ATPase and transport rates and facilitated conformational trapping for structural studies. In the substrate-bound state, a single molecule of estrone-3-sulfate (E_1S) is bound in a central, hydrophobic and cytoplasm-facing cavity about halfway across the membrane. Only one molecule of E_1S can bind in the observed binding mode. In the ATP-bound state, the substrate-binding cavity has collapsed while an external cavity has opened to the extracellular side of the membrane. The ATP-induced conformational changes include rigid-body shifts of the transmembrane domains, pivoting of the nucleotide-binding domains (NBDs), and a change in the relative orientation of the NBD subdomains. Mutagenesis and in vitro characterization of transport and ATPase activities demonstrate the roles of specific residues in substrate recognition, including a leucine residue that forms a 'plug' between the two cavities. Our results show how ABCG2 harnesses the energy of ATP binding to extrude E_1S and other substrates, and suggest that the size and binding affinity of compounds are important for distinguishing substrates from inhibitors.

We first established that replacing the catalytic glutamate E211 with a glutamine in the Walker B motif (a phosphate-binding sequence) resulted in greatly reduced, but not abolished, ATP hydrolysis and E_1S transport activity[13] (Fig. 1 and Extended Data Fig. 1). Next, to determine the E_1S-bound structure ($ABCG2_{EQ}$–E_1S), we added the antigen-binding fragment of the monoclonal antibody 5D3 (5D3-Fab) to the sample, which bound to the external side of ABCG2 and facilitated the determination of the high-resolution structure[15]. 5D3-Fab inhibits the transport activity of liposome-reconstituted ABCG2 and slows down its ATP hydrolysis, but has no effect on the half-maximal effective concentration (EC_{50}) of E_1S-induced ATPase stimulation, suggesting that it does not alter the interaction between ABCG2 and E_1S[13,16] (Extended Data Fig. 2). The predominant three-dimensional (3D) class of nanodisc-reconstituted $ABCG2_{EQ}$–E_1S revealed an inward-open conformation and was refined to an overall resolution of 3.6 Å, such that the transmembrane domains (TMDs)—including the substrate-binding cavity—were clearly resolved (Extended Data Figs. 3, 4a and Extended Data Table 1). We observed a density feature in the substrate-binding cavity, which is formed by transmembrane (TM) helices TM2 and TM5a of opposing ABCG2 monomers. The density could fit only one E_1S molecule but given that ABCG2 has two-fold symmetry, E_1S can be bound in two orientations related by a 180° rotation (Fig. 2a, b and Extended Data Fig. 4b). Two E_1S molecules cannot bind simultaneously because their polycyclic ring systems would clash sterically. The strongest density was at the two-fold symmetry axis, where the core of the flat polycyclic ring binds, and reprocessing the data with C1 symmetry resulted in a very similar—albeit lower-resolution—electron microscopy map (Extended Data Fig. 4b, c). The substrate-binding cavity was shown previously to accommodate potent inhibitors, demonstrating its dual role in substrate and multidrug binding[14] (Fig. 2c).

The $ABCG2_{EQ}$–E_1S structure revealed which residues interacted with bound substrate (Fig. 2d). We generated single point mutations of all of these residues, and determined the in vitro ATPase and E_1S transport activities of the resulting ABCG2 variants upon reconstitution of the purified proteins in proteoliposomes (Fig. 2e, f). The stability of all mutants tested was similar to that of the wild-type protein (Extended Data Fig. 5a), allowing direct comparison. We also determined the EC_{50} values of E_1S-induced ATPase stimulation for all mutants (Extended Data Fig. 5b, c). Consistent with their role in binding E_1S, the transport activities of the mutants N436A and F439A were strongly reduced, as were their ATPase activities. Notably, neither the N436A nor the F439A mutant showed stimulation of their ATPase activity by E_1S, indicating that the interactions suggested by the structure (a hydrogen bond between N436 and the sulfate group of E_1S, and the stacking interaction of the phenyl ring of F439 to the ring system of E_1S) are important for substrate binding (Fig. 2 and Extended Data Fig. 5b, c). The V546F mutant had impaired transport activity but displayed a 12-fold increase in basal ATPase activity, which was inhibited by E_1S in a concentration-dependent manner. This could suggest that the introduction of two phenyl rings at this position of the substrate-binding cavity mimics the binding of a substrate and thus stimulates ATPase activity, whereas further addition of E_1S 'clogs' the transporter.

The V546A mutant, by contrast, had similar functional characteristics to the wild-type protein, with a slight increase in the EC_{50} of E_1S stimulation. It has previously been reported that in the ABCG5/ABCG8 heterodimeric protein, the mutations Y432A and A540F (equivalent to F439A and V546F in ABCG2) disrupted cholesterol transport[17], suggesting a common location for the substrate-binding site among G-subfamily ABC transporters. We further found that the mutation T435A caused a roughly 4.5-fold increase in the apparent EC_{50} of ATPase stimulation, consistent with our interpretation from the structure that a hydrogen bond exists between the β-hydroxyl group of T435 and the ester group of E_1S. There was a twofold increase in transport in the T435A mutant, suggesting an inverse relationship between binding affinity and the maximal transport rate. The introduction of two phenylalanines (T435F mutant) impaired both E_1S transport and ATP hydrolysis—a different effect to that seen with V546F. This emphasizes the sensitivity of the binding cavity to modifications. Finally, the M549A mutant had similar ATPase and transport activities

[1]Institute of Molecular Biology and Biophysics, Department of Biology, ETH Zurich, Switzerland. [2]Center for Cellular Imaging and NanoAnalytics (C-CINA), Biozentrum, University of Basel, Basel, Switzerland. [3]Novo Nordisk Foundation Center for Protein Research, Faculty of Health and Medical Sciences, University of Copenhagen, Copenhagen, Denmark. [4]These authors contributed equally: Ioannis Manolaridis, Scott M. Jackson, Nicholas M. I. Taylor, Julia Kowal. *e-mail: henning.stahlberg@unibas.ch; locher@mol.biol.ethz.ch

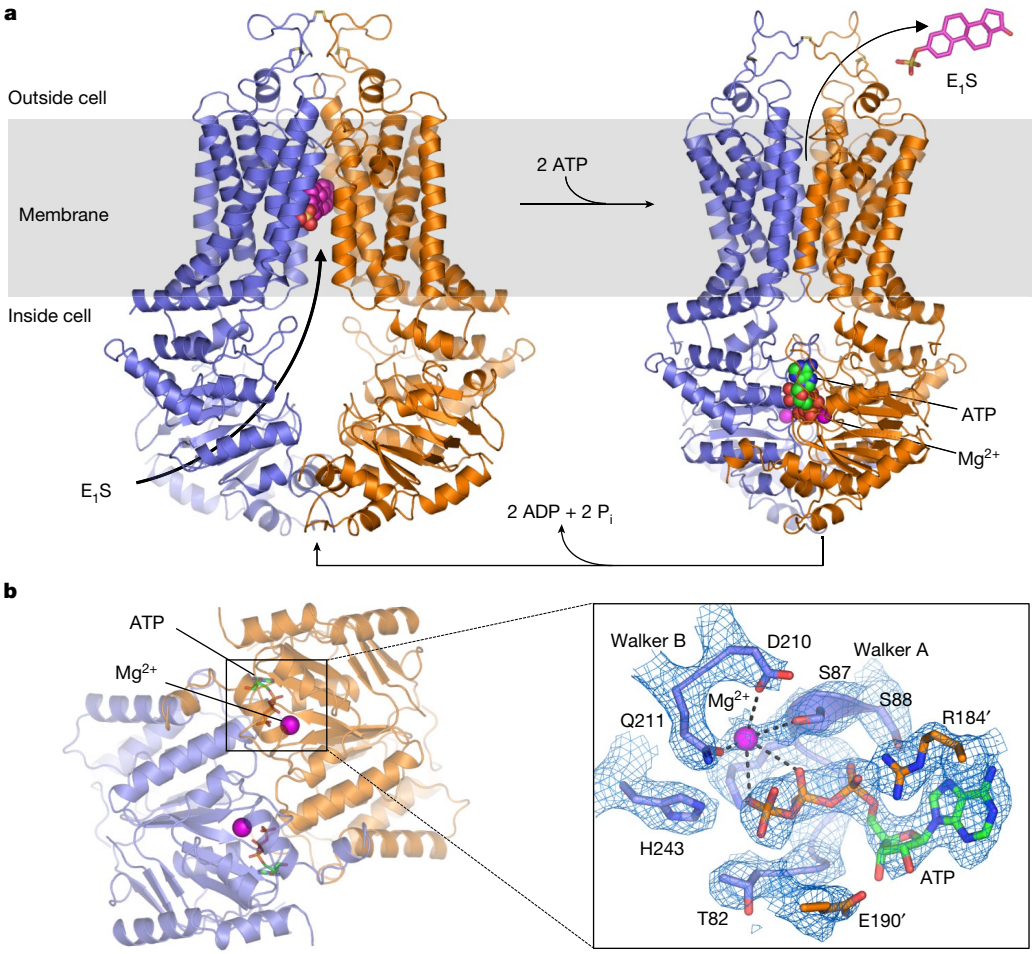

Fig. 1 | Structures and transport cycle of ABCG2. a, Cartoon representation of $ABCG2_{EQ}$–E_1S (left) and $ABCG2_{EQ}$–ATP (right). ABCG2 monomers coloured blue and orange. Bound E_1S, ATP and Mg^{2+} shown as spheres. In $ABCG2_{EQ}$–E_1S, bound 5D3-Fab omitted for clarity. **b**, Structure of NBD dimer from the ATP-bound state, viewed from the cytoplasm, with bound ATP (sticks) and Mg^{2+} ions (spheres). Inset (rotated about 150° to the right, viewed from the membrane): electron microscopy density around bound ATP, with Walker A and Walker B motifs, E190 of the signature motif and the 'switch' histidine (H243) shown as sticks and labelled; Mg^{2+} shown as purple sphere.

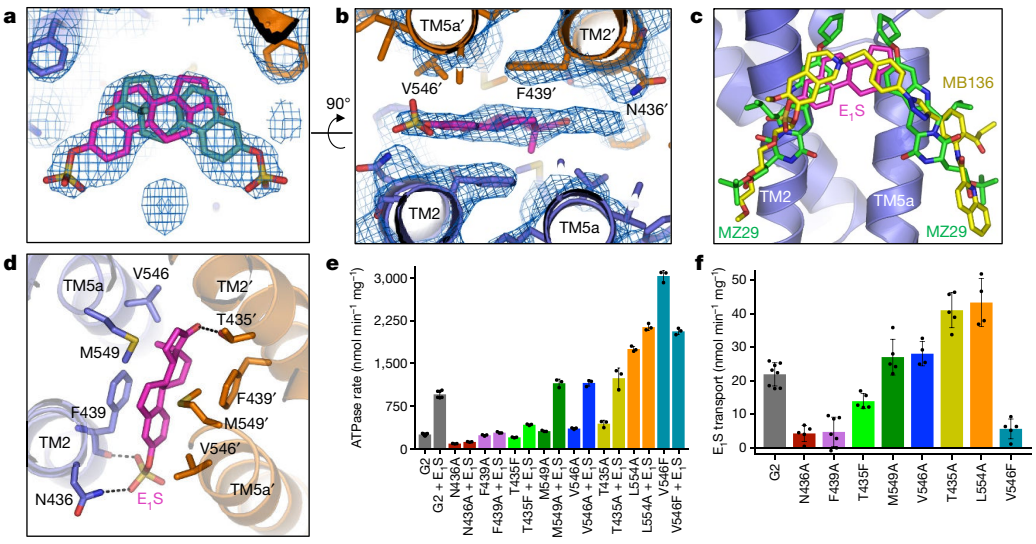

Fig. 2 | Substrate-binding cavity and mutant analysis. a, C2-symmetrized electron microscopy density of $ABCG2_{EQ}$–E_1S; bound E_1S molecule (pink or turquoise sticks) shown in two possible orientations, rotated by 180° along *y*-axis. **b**, As in **a**, but rotated 90° and showing one E_1S molecule and surrounding residues as viewed from the cytoplasm. TM helices and contacting residues are labelled. **c**, Overlay of E_1S (pink sticks; this study) and inhibitors MZ29 (green sticks; Protein Data Bank accession number (PDB): 6ETI) and MB136 (yellow sticks; PDB: 6FEQ), bound in the substrate-binding cavity, after superposition of the three structures. **d**, Substrate-binding cavity viewed from within the membrane, showing side chains (sticks) of residues interacting with E_1S (pink sticks). **e**, ATPase activities of liposome-reconstituted wild-type and mutant ABCG2 in the presence and absence of 50 μM E_1S. **f**, Initial E_1S-transport activities. The bars show means; error bars show standard deviations; and dots show rates derived from each technical replicate (same batch of liposomes).

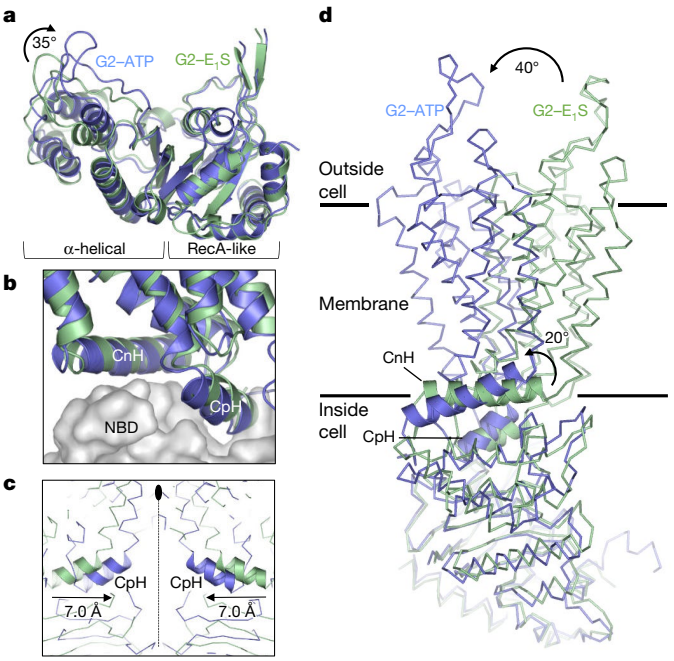

Fig. 3 | ATP-induced conformational changes. a, Superposition of the RecA-like subdomains of the NBDs of the $ABCG2_{EQ}$–E_1S (green) and $ABCG2_{EQ}$–ATP (blue) structures. A roughly 35° inward rotation of the helical subdomain is observed upon ATP binding. **b**, Superposition of one ABCG2 monomer of the $ABCG2_{EQ}$–E_1S and $ABCG2_{EQ}$–ATP structures, with the NBDs shown as a grey surface and the TMDs as ribbons. The interface helices—CpH and CnH—are labelled. **c**, Superposition of the $ABCG2_{EQ}$–E_1S and $ABCG2_{EQ}$–ATP structures along the two-fold symmetry axis (dotted line), showing a 7 Å inward movement of the CpH helices of each ABCG2 monomer. **d**, Comparison of a single ABCG2 monomer of the $ABCG2_{EQ}$–E_1S and $ABCG2_{EQ}$–ATP structures. The NBDs have been superimposed, revealing a 20° rotation of the CnH and CpH helices (shown as ribbons) as well as a 40° rotation of the TMDs relative to one another.

to the wild-type protein, suggesting a minor contribution of this residue to E_1S binding.

To visualize ATP-driven conformational changes in ABCG2, we added ATP and magnesium to nanodisc-reconstituted $ABCG2_{EQ}$ in the absence of 5D3-Fab ($ABCG2_{EQ}$–ATP). Cryo-EM analysis revealed that most particles featured an ATP-bound conformation with the NBD dimer closed, and no inward-facing classes (Fig. 1 and Extended Data Fig. 6). The overall resolution was 3.1 Å, with excellent side-chain density for the TMDs, NBDs and nucleotides (Extended Data Fig. 4d and Extended Data Table 1). The structure revealed a closed, 'head-to-tail' NBD dimer, featuring a much larger interface than in the nucleotide-free state, and forming two ATP-binding sites between the Walker A motif (another phosphate-binding loop, or P-loop) of one NBD and the signature sequence (VSGGE sequence) of the other (Fig. 1b). ATP molecules are bound, and there is clear electron microscopy density for a magnesium ion interacting with the β- and γ-phosphates of each ATP (Fig. 1b). Three conserved side chains coordinate the γ-phosphate of ATP: Q211 (corresponding to the catalytic glutamate in wild-type ABCG2); H243 (corresponding to the 'switch' histidine[18]); and Q126 (which is part of the Q-loop). Q211 also coordinates the magnesium ion. ABCG2 does not contain an A-loop with an aromatic side chain stacking against the adenine moiety, as is seen in many other ABC transporters[19–22]. Rather, one face of the adenine ring is in Van der Waals distance of residues V46, I63 and G185 from one NBD; the other face stacks against R184 from the opposite NBD. R184 also forms a salt bridge with the α-phosphate, which was observed previously in the AMPPNP-bound structure of the bacterial B12 transporter BtuCDF[23]. The NBD interface of ATP-bound $ABCG2_{EQ}$ also contains a salt bridge formed by E127 (part of the Q-loop) and R191 adjacent to the signature motif. Unlike in B-family ABC transporters, there is a hole at the interface of the four domains of ABCG2, rather similar to what was seen in BtuCDF (Fig. 1a).

As a result of ATP binding, the α-helical domains of the NBDs have rotated by roughly 35° relative to the RecA-like domains, approaching the opposite NBD and the two-fold symmetry axis (Fig. 3a). This rotation is required for NBD dimerization and is part of the 'power stroke' in the transport cycle[24]. The individual TMD–NBD interfaces—formed mainly by the 'connecting helices' (CnH or TM1a) and 'coupling helices' (CpH, corresponding to the carboxy-terminal part of TM2)—remain largely unchanged in each ABCG2 monomer between the nucleotide-free and ATP-bound states (Fig. 3b). However, because of the shift in the NBDs, the cytoplasmic parts of the TMDs are pushed towards each other, with each CpH approaching the two-fold symmetry axis by around 7 Å (Fig. 3c). The altered conformations of the TMDs can be described as rigid-body movements, with CnH and CpH acting as the pivot points for the transition. These two α-helices undergo a roughly 20° rotation when superposing the NBDs in the structures of the two states, which translates to a roughly 40° rotation of the helical axes of the TMDs (Fig. 3d).

The ATP-induced conformational changes have important consequences for the substrate-translocation pathway. In the $ABCG2_{EQ}$–E_1S structure, the phenyl rings of the F439 residues of the two ABCG2 monomers are 8.0 Å apart, with bound E_1S between them (Fig. 2d). By contrast, these phenyl rings stack against each other in the ATP-bound state (Fig. 4a, c) and the substrate-binding cavity has completely collapsed, with no space for bound substrate. To be transported across the membrane, therefore, the substrate has to move through the likely translocation pathway at the centre of the transporter and reach the external cavity before the pathway is completely closed. This can be accomplished only if there are transient conformational changes such as TM-helix bending, to generate space for the substrate. Such transient changes resemble a peristaltic motion.

The external cavity—occluded in the nucleotide-free state—is open to the outside in the ATP-bound state, while maintaining the intra- and intermolecular disulfides (C592–C608 and C603–C603′) in extracellular loop 3 (EL3), promoting substrate release (Figs. 1a, 4d and Extended Data Figs. 1b, 6e). Two leucine residues (L554 and L555), in the loop between TM5a and TM5b, form a plug that separates the substrate-binding cavity and the external cavity (Fig. 4). We individually mutated these leucines to alanines and found that the L555A variant did not express any functional protein, suggesting a structural role of L555 in addition to a likely gating function. By contrast, the L554A mutant was stable and showed functional differences compared to wild-type ABCG2 (Fig. 2e, f and Extended Data Fig. 5): the basal ATPase rate of L554A was greatly increased and there was only a minor stimulation of the ATPase rate by E_1S (around 20%, compared with roughly 3.5-fold in wild-type ABCG2). Furthermore, the apparent EC_{50} of E_1S-induced ATPase stimulation was increased, suggesting weaker substrate binding. Finally, the E_1S transport activity of the L554A mutant was twice as high as that of wild-type ABCG2. We interpret that the opening and closing of the 'leucine plug' may act as a checkpoint during the transport reaction, and that although the removal of the leucine side chain accelerates the transport process, it may reduce substrate selectivity.

A comparison of the structures shown here provides insight into the transport cycle of ABCG2. Substrate may bind via the cytoplasm or from within the lipid bilayer via the 'membrane entrance'[14] (Fig. 4b). Once substrate is bound, the NBD dimer can only close when the substrate moves out of the substrate-binding cavity, because this cavity does not provide any space when ATP is also bound. In a productive transport cycle, substrate probably moves through a translocation pathway at the centre of the transporter, via the 'leucine plug'. The structure of ATP-bound $ABCG2_{EQ}$ suggests that once a substrate clears the plug area and enters the external cavity, the plug region closes and substrate is released to the outside (Fig. 4d). One caveat is that the E211Q mutation may have influenced the energetics of the conformational changes

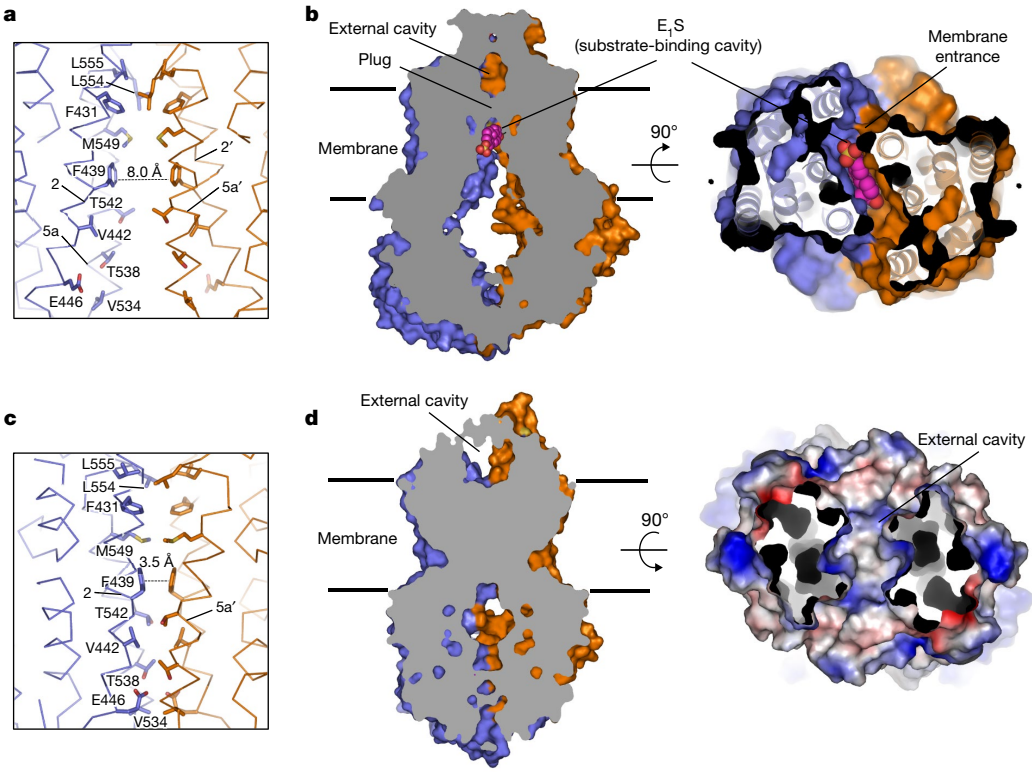

Fig. 4 | Substrate-translocation pathway. a, Cα trace of the translocation-pathway region of $ABCG2_{EQ}$–E_1S. Residues lining the substrate-binding cavity are shown as sticks; bound E_1S has been omitted for clarity. The dashed line shows the distance between the two F439 residues that stack against bound E_1S. **b**, Vertical slice through a surface representation of $ABCG2_{EQ}$–E_1S, with bound E_1S shown as pink spheres and the two cavities and plug region labelled. In the right-hand panel, a 90° rotation of the structure reveals the fit of E_1S in the substrate-binding cavity, as viewed from the cytoplasm. The NBDs have been removed for clarity. **c**, **d**, As for **a**, **b**, but with the $ABCG2_{EQ}$–ATP structure. In the right-hand panel of **d**, the molecular surface of the external cavity, viewed from the extracellular space and colour-coded by electrostatic potential ranging from blue (most positive) to red (most negative), is shown with the extracellular loop EL3 removed for clarity.

involved. Our findings suggest that ATP binding might be sufficient for the substrate-extrusion step and that ATP hydrolysis might be required to reset the transporter to an inward-facing conformation[19,20,25,26]. Unlike many other transporters[22,27–30], ABCG2 does not appear to form a stable, occluded conformation providing space for bound substrate, but rather a transient conformation that is consistent with a peristalsis-like mechanism, reminiscent of the bacterial BtuCDF transporter.

Given their polyspecificity, a key unanswered question concerning multidrug transporters such as ABCG2 is why certain compounds act as substrates, while others are potent inhibitors. Our results allow us to compare the binding modes of a bona fide ABCG2 substrate with those of two potent inhibitors. All three molecules bind in the same cavity of the transporter (Fig. 2c). However, whereas a single E_1S molecule binds on the two-fold symmetry axis and deep in the cavity, two molecules of MZ29—a compound derived from the ABCG2 inhibitor Ko143—have been found to fill the substrate-binding cavity completely, almost reaching the cytoplasmic membrane boundary and forming many additional contacts with the surface of ABCG2 (ref. [14]). A single copy of the tariquidar-derived inhibitor MB136 also fills the binding cavity completely, forming similar contacts to MZ29. The numerous additional contacts, which include residues of TM1b in addition to TM2 and TM5a, can explain the increased binding affinity of inhibitors compared with substrates. The difference appears to mean that when E_1S and ATP are bound to ABCG2, the NBDs and the cytoplasmic part of the TMDs can still approach, allowing for an opening of the plug and simultaneous pushing of the substrate into the external cavity. Inhibitors, by contrast, act as 'wedges' and immobilize the transporter by locking it in an inward-facing conformation. The reduced size, binding surface and affinity of substrates, and their binding deeper inside the substrate cavity, allow them to be translocated in a productive transport cycle.

Online content

Any methods, additional references, Nature Research reporting summaries, source data, statements of data availability and associated accession codes are available at https://doi.org/10.1038/s41586-018-0680-3.

Received: 26 March 2018; Accepted: 24 August 2018;
Published online 7 November 2018.

1. Diestra, J. E. et al. Frequent expression of the multi-drug resistance-associated protein BCRP/MXR/ABCP/ABCG2 in human tumours detected by the BXP-21 monoclonal antibody in paraffin-embedded material. *J. Pathol.* **198**, 213–219 (2002).
2. Fetsch, P. A. et al. Localization of the ABCG2 mitoxantrone resistance-associated protein in normal tissues. *Cancer Lett.* **235**, 84–92 (2006).
3. Robey, R. W. et al. ABCG2: a perspective. *Adv. Drug Deliv. Rev.* **61**, 3–13 (2009).
4. Vlaming, M. L., Lagas, J. S. & Schinkel, A. H. Physiological and pharmacological roles of ABCG2 (BCRP): recent findings in Abcg2 knockout mice. *Adv. Drug Deliv. Rev.* **61**, 14–25 (2009).
5. Gillet, J. P. & Gottesman, M. M. Advances in the molecular detection of ABC transporters involved in multidrug resistance in cancer. *Curr. Pharm. Biotechnol.* **12**, 686–692 (2011).
6. Gottesman, M. M., Fojo, T. & Bates, S. E. Multidrug resistance in cancer: role of ATP-dependent transporters. *Nat. Rev. Cancer* **2**, 48–58 (2002).
7. Imai, Y. et al. Breast cancer resistance protein exports sulfated estrogens but not free estrogens. *Mol. Pharmacol.* **64**, 610–618 (2003).
8. Ishikawa, T., Aw, W. & Kaneko, K. Metabolic interactions of purine derivatives with human ABC transporter ABCG2: genetic testing to assess gout risk. *Pharmaceuticals* **6**, 1347–1360 (2013).
9. Mao, Q. & Unadkat, J. D. Role of the breast cancer resistance protein (BCRP/ABCG2) in drug transport—an update. *AAPS J.* **17**, 65–82 (2015).
10. Mo, W. & Zhang, J. T. Human ABCG2: structure, function, and its role in multidrug resistance. *Int. J. Biochem. Mol. Biol.* **3**, 1–27 (2012).
11. Sarkadi, B., Homolya, L., Szakács, G. & Váradi, A. Human multidrug resistance ABCB and ABCG transporters: participation in a chemoimmunity defense system. *Physiol. Rev.* **86**, 1179–1236 (2006).

12. Sharom, F. J. The P-glycoprotein multidrug transporter. *Essays Biochem*. **50**, 161–178 (2011).
13. Taylor, N. M. I. et al. Structure of the human multidrug transporter ABCG2. *Nature* **546**, 504–509 (2017).
14. Jackson, S. M. et al. Structural basis of small-molecule inhibition of human multidrug transporter ABCG2. *Nat. Struct. Mol. Biol*. **25**, 333–340 (2018).
15. Zhou, S. et al. The ABC transporter Bcrp1/ABCG2 is expressed in a wide variety of stem cells and is a molecular determinant of the side-population phenotype. *Nat. Med*. **7**, 1028–1034 (2001).
16. Suzuki, M., Suzuki, H., Sugimoto, Y. & Sugiyama, Y. ABCG2 transports sulfated conjugates of steroids and xenobiotics. *J. Biol. Chem*. **278**, 22644–22649 (2003).
17. Lee, J. Y. et al. Crystal structure of the human sterol transporter ABCG5/ABCG8. *Nature* **533**, 561–564 (2016).
18. Hanekop, N., Zaitseva, J., Jenewein, S., Holland, I. B. & Schmitt, L. Molecular insights into the mechanism of ATP-hydrolysis by the NBD of the ABC-transporter HlyB. *FEBS Lett*. **580**, 1036–1041 (2006).
19. Johnson, Z. L. & Chen, J. ATP binding enables substrate release from multidrug resistance protein 1. *Cell* **172**, 81–89 (2018).
20. Kim, Y. & Chen, J. Molecular structure of human P-glycoprotein in the ATP-bound, outward-facing conformation. *Science* **359**, 915–919 (2018).
21. Shintre, C. A. et al. Structures of ABCB10, a human ATP-binding cassette transporter in apo- and nucleotide-bound states. *Proc. Natl Acad. Sci. USA* **110**, 9710–9715 (2013).
22. Zhang, Z., Liu, F. & Chen, J. Conformational changes of CFTR upon phosphorylation and ATP binding. *Cell* **170**, 483–491 (2017).
23. Korkhov, V. M., Mireku, S. A. & Locher, K. P. Structure of AMP-PNP-bound vitamin B12 transporter BtuCD-F. *Nature* **490**, 367–372 (2012).
24. Zaitseva, J. et al. A structural analysis of asymmetry required for catalytic activity of an ABC-ATPase domain dimer. *EMBO J*. **25**, 3432–3443 (2006).
25. Aller, S. G. et al. Structure of P-glycoprotein reveals a molecular basis for poly-specific drug binding. *Science* **323**, 1718–1722 (2009).
26. Johnson, Z. L. & Chen, J. Structural basis of substrate recognition by the multidrug resistance protein MRP1. *Cell* **168**, 1075–1085 (2017).
27. Alam, A. et al. Structure of a zosuquidar and UIC2-bound human-mouse chimeric ABCB1. *Proc. Natl Acad. Sci. USA* **115**, E1973–E1982 (2018).
28. Choudhury, H. G. et al. Structure of an antibacterial peptide ATP-binding cassette transporter in a novel outward occluded state. *Proc. Natl Acad. Sci. USA* **111**, 9145–9150 (2014).
29. Hohl, M., Briand, C., Grütter, M. G. & Seeger, M. A. Crystal structure of a heterodimeric ABC transporter in its inward-facing conformation. *Nat. Struct. Mol. Biol*. **19**, 395–402 (2012).
30. Verhalen, B. et al. Energy transduction and alternating access of the mammalian ABC transporter P-glycoprotein. *Nature* **543**, 738–741 (2017).

Acknowledgements This research was supported by the Swiss National Science Foundation through the National Centre of Competence in Research (NCCR) TransCure and by a Swiss Federal Institute of Technology Zurich (ETH Zurich) research grant (ETH-22-14-1). N.M.I.T. was also supported by the Research Fund Junior Researchers of the University of Basel. J.K. was also supported by the TransCure Young Investigator Award (2017). Cryo-EM data were collected at C-CINA, University of Basel; we thank K. Goldie, L. Kováčik and A. Fecteau-Lefebvre for technical support. We thank N. Tremp for help with cell culture and B. Sorrentino (St Jude Children's Research Hospital) for providing the 5D3-producing hybridoma cell line.

Reviewer information *Nature* thanks H. Mchaourab and the other anonymous reviewer(s) for their contribution to the peer review of this work.

Author contributions I.M. expressed and purified wild-type ABCG2 and 5D3-Fab. I.M. and S.M.J. cloned, expressed and purified the ABCG2 mutants. S.M.J. reconstituted ABCG2 into liposomes and lipidic nanodiscs for cryo-EM and functional studies and carried out all functional experiments. J.K. prepared cryo-grids. N.M.I.T. collected cryo-EM data with the assistance of H.S. I.M. processed cryo-EM data of ATP-bound ABCG2 and determined the structure with the assistance of J.K. N.M.I.T. processed electron microscopy data and determined the structure of E_1S-bound ABCG2. I.M and K.P.L. built, refined and validated the structures. K.P.L., I.M. and S.M.J. conceived the project, designed the experiments and wrote the manuscript. All authors contributed to revision of the manuscript.

Competing interests The authors declare no competing interests.

Additional information
Extended data is available for this paper at https://doi.org/10.1038/s41586-018-0680-3.
Supplementary information is available for this paper at https://doi.org/10.1038/s41586-018-0680-3.
Reprints and permissions information is available at http://www.nature.com/reprints.
Correspondence and requests for materials should be addressed to H.S. or K.P.L.
Publisher's note: Springer Nature remains neutral with regard to jurisdictional claims in published maps and institutional affiliations.

METHODS

No statistical methods were used to predetermine sample size. The experiments were not randomized. The investigators were not blinded to allocation during experiments and outcome assessment.

Expression and purification of wild-type and mutant human ABCG2. Human ABCG2, containing an amino (N)-terminal Flag tag, was expressed in HEK293-EBNA (Thermo Fisher Scientific) cells and purified as described[13,14].

Expression and purification of 5D3-Fab. 5D3 hybridoma cells, producing the 5D3 monoclonal antibody, were obtained from B. Sorrentino. The cells were cultured in WHEATON CELLine Bioreactors, according to the manufacturer's protocol, and 5D3-Fab was then purified from the supernatant, as described in the Fab Preparation Kit protocol (Thermo Fisher Scientific).

Nanodisc preparation of $ABCG2_{EQ}$. The membrane scaffold protein (MSP) 1D1 was expressed and purified[31] and ABCG2 was reconstituted into brain polar lipid (BPL)/cholesterol hemisuccinate (CHS) nanodiscs as described[13,14]. To generate the $ABCG2_{EQ}$–E_1S sample for cryo-EM studies, ABCG2 was first mixed with a threefold molar excess of 5D3-Fab before reconstitution. After size-exclusion chromatography (SEC) using a Superdex 200 10/300 column (GE Healthcare), the complex was incubated with 200 μM E_1S, 5 mM ATP and 5 mM $MgCl_2$ for 15 min at room temperature before grid preparation. For the $ABCG2_{EQ}$–ATP sample, following SEC, the complex was incubated with 5 mM ATP and 5 mM $MgCl_2$ for 15 min at room temperature before grid preparation.

ABCG2 liposome preparation. A BPL/cholesterol (Avanti Polar Lipids) mixture was prepared at a 4/1 (w/w) ratio as described[32]. Detergent-purified ABCG2 was then mixed with BPL/cholesterol; detergent was removed with Bio-Beads and the reconstitution efficiency determined[13,14,33].

Transport assays. In vitro transport assays using ABCG2 proteoliposomes, containing either wild-type or mutant protein, were carried out as described. In brief, ABCG2 proteoliposomes were extruded and then incubated with 5 mM $MgCl_2$ and 50 μM [^{3}H]-E_1S for 5 min at 30 °C. The transport reaction was initiated by the addition of 2 mM ATP and the sample was filtered using a Multiscreen vacuum manifold (MSFBN6B filter plate, Millipore). Radioactivity trapped on the filters was measured using a scintillation counter and the initial transport rates (over 30 seconds to 2 minutes) were determined using linear regression in GraphPad Prism 7.00. Rates were corrected for the orientation of ABCG2 in proteoliposomes[13,14].

ATPase assays and determination of the EC_{50} of E_1S stimulation. ATP-hydrolysis activity was measured using a previously described technique[34]. All reactions were performed at 37 °C in the presence of 2 mM ATP and 10 mM $MgCl_2$[13,14]. For ATPase assays in proteoliposomes, experiments were completed in the presence of 0–300 μM E_1S. To assess the effect of 5D3-Fab, ABCG2 proteoliposomes were freeze-thawed five times in the presence of a threefold molar excess of 5D3-Fab (to ensure that the antibody was present inside the proteoliposomes) before extrusion. Assays in nanodiscs were performed in the absence of E_1S. Data were recorded at four time intervals (0, 5, 15 and 30 min) and subsequent ATPase rates were determined using linear regression in GraphPad Prism 7.00. Rates were corrected for the orientation of ABCG2 in proteoliposomes. To determine the EC_{50} of E_1S stimulation, we plotted the ATPase rates against the E_1S concentration, and generated curves using the nonlinear regression Michaelis–Menten analysis tool in GraphPad Prism 7.00.

Sample preparation and cryo-EM data acquisition. All cryo grids of $ABCG2_{EQ}$ were prepared using a Vitrobot Mark IV (FEI) with the environmental chamber set at 100% humidity and 4 °C. An aliquot of 4 μl purified $ABCG2_{EQ}$–E_1S or $ABCG2_{EQ}$–ATP, at a protein concentration of approximately 0.4 mg ml^{-1}, was applied to glow-discharged Quantifoil (1.2/1.3) 300-mesh copper grids. After being blotted with filter paper for 2.0 s, the grids were flash-frozen in a mixture of propane and ethane cooled with liquid nitrogen. The $ABCG2_{EQ}$–E_1S dataset was composed of 3,984 movies and the $ABCG2_{EQ}$–ATP dataset was composed of 4,905 movies. Cryo-EM image data were recorded using SerialEM[35] on a Titan Krios microscope, operated at 300 kV and equipped with a Gatan Quantum-LS energy filter (20 eV zero loss filtering), containing a K2 Summit direct electron detector. Images were recorded in super-resolution counting mode with a pixel size of 0.4058 Å per pixel. Exposures were 10 s, dose-fractionated into 50 frames (0.2 s per frame), resulting in a frame dose of 2.0 electrons per Å^2. Data-collection quality was monitored using Focus[36]. The first frame of each movie was discarded. Stacks were gain-normalized, motion-corrected, dose-weighted and averaged and then Fourier-cropped twofold with MotionCor2 (ref. [37]). Defocus estimates were obtained on the non-dose-weighted micrographs with CTFFIND4 (ref. [38]) for $ABCG2_{EQ}$–E_1S and Gctf[39] for $ABCG2_{EQ}$–ATP.

Image processing. Particles were picked automatically using Gautomatch (http://www.mrc-lmb.cam.ac.uk/kzhang/), resulting in an $ABCG2_{EQ}$–E_1S dataset of 168,184 particles—processed with CryoSPARC[40]—and an $ABCG2_{EQ}$–ATP dataset of 1,128,170 particles, processed with RELION[41]. In both cases, 2D classification yielded at least 12 representative classes, containing 62,616 particles for $ABCG2_{EQ}$–E_1S and 543,142 particles for $ABCG2_{EQ}$–ATP. These classes were used for ab initio reconstruction (applying either C1 or C2 symmetry).

For $ABCG2_{EQ}$–E_1S, the resulting 3D models were used as a starting point for heterogeneous 3D refinement with three classes. Subsequent homogeneous refinements of all three classes (applying C2 symmetry) separately yielded maps that were very alike, with the maps for the two largest classes (corresponding to 38.7% and 32.6% of particles) having very similar densities in the substrate-binding cavity of ABCG2, and the map of smaller class (corresponding to 28.5% of the particles) having some additional density underneath the substrate density (which was only visible at noise level in the other classes). Therefore, we combined particles of the two largest classes (42,790 particles in total) from the 3D heterogeneous refinement and refined (applying C2 symmetry) against the heterogeneous refinement map of the largest class. This resulted in a map with a resolution of 3.58 Å, which was sharpened with an automatically calculated B-factor of −82.6 Å^2. For validation, all refinements were also performed using C1 symmetry.

For $ABCG2_{EQ}$–ATP, initial 3D classification into three classes resulted in one outstanding class, containing 51.8% of particles (corresponding to 288,447 particles) with clear secondary-structure elements. This class was 3D-refined, applying C2 symmetry and a soft mask, resulting in a 3D reconstruction with an overall resolution of 3.14 Å. For nanodisc subtraction, the $ABCG2_{EQ}$–ATP map was segmented in Chimera (using Segger) and the resulting nanodisc-only map was used to calculate projections, which were subsequently subtracted from the experimental particles. A soft mask, in which the subtracted density from the experimental particles was white (1) and the rest of the protein and the solvent were black (0), was generated by low-passing the nanodisc map to 15 Å and expanding the mask by 4 pixels with a soft edge of 6 pixels. The nanodisc-free experimental particles were used in further 3D refinements, which resulted in an electron microscopy map at a resolution of 3.09 Å (B-factor of −136 Å^2), using the low-passed $ABCG2_{EQ}$–ATP map without nanodisc density as a reference. This map was used for $ABCG2_{EQ}$–ATP model building. Subsequent 3D classification in C1 symmetry, without applied alignments, was carried out in an effort to improve the EL3 density; however, despite extensive efforts the inherent flexibility of EL3 in this conformation prohibited its accurate modelling.

All resolutions were estimated with the Fourier shell correlation (FSC) 0.143 cut-off criterion[42]. ResMap[43] was used to calculate the local resolution maps.

Model building and refinement. For the $ABCG2_{EQ}$–E_1S structure, we used the post-processed map at an overall resolution of 3.58 Å. To generate an initial model, we docked the ABCG2–MZ29–Fab structure (Protein Data Bank 6ETI) into the electron microscopy density using Coot[44], and carried out manual fitting and modifications where the resolution allowed. The E_1S coordinates and restraints were generated using eLBOW[45] and fitted into the electron microscopy density using Coot. For the $ABCG2_{EQ}$–ATP structure, we used the post-processed, nanodisc-subtracted map at an overall resolution of 3.09 Å. The electron microscopy density was of excellent quality and allowed for the accurate building of ABCG2, ATP and magnesium from the ligand library in Coot, using the ABCG2–MZ29–Fab structure (PDB: 6ETI) as a template. For both structures, the complete models were refined against the working maps in PHENIX[46] using the program phenix.real_space_refine. For the final round of model refinement, we performed global real-space refinement with standard geometry restraints as well as rotamer, Ramachandran plot, C-beta, non-crystallographic symmetry and secondary-structure restraints, coupled to reciprocal-space refinement of the B-factors. The quality of the final models was analysed by MolProbity[47] and the refinement statistics are given in Extended Data Table 1. To validate the refinement, we introduced random shifts (mean value of 0.3 Å) into the coordinates of the final refined models using the program phenix.pdbtools[46], followed by refinement with phenix.real_space_refine (using the same parameters as described before) against the first unfiltered half-map (half-map 1). The overlay between the FSC curve of the model with random displacements refined against half-map1 versus half-map 1 and the FSC curve of the same model versus half-map 2 (against which it was not refined) indicated that no over-refinement took place.

Figure preparation. Figures were prepared using the programs PyMOL (PyMOL Molecular Graphics System, DeLano Scientific) and GraphPad Prism 7.00 (GraphPad Software).

Reporting summary. Further information on experimental design is available in the Nature Research Reporting Summary linked to this paper.

Data availability

Atomic coordinates for $ABCG2_{EQ}$–E_1S (including only the variable domain of 5D3-Fab) and $ABCG2_{EQ}$–ATP were deposited in the Protein Data Bank under accession codes 6HCO and 6HBU, respectively. Electron microscopy data for the two structures were deposited in the Electron Microscopy Data Bank under accession codes EMD-0196 ($ABCG2_{EQ}$–E_1S) and EMD-0190 ($ABCG2_{EQ}$–ATP). Source Data for Fig. 2e, f and Extended Data Figs. 1e, 2b, d, f and 5 are available online. All other data are available from the corresponding author upon reasonable request. A Life Sciences Reporting Summary for this article is available.

31. Ritchie, T. K. et al. Chapter 11—reconstitution of membrane proteins in phospholipid bilayer nanodiscs. *Methods Enzymol.* **464**, 211–231 (2009).
32. Geertsma, E. R., Nik Mahmood, N. A., Schuurman-Wolters, G. K. & Poolman, B. Membrane reconstitution of ABC transporters and assays of translocator function. *Nat. Protocols* **3**, 256–266 (2008).
33. Schaffner, W. & Weissmann, C. A rapid, sensitive, and specific method for the determination of protein in dilute solution. *Anal. Biochem.* **56**, 502–514 (1973).
34. Chifflet, S., Torriglia, A., Chiesa, R. & Tolosa, S. A method for the determination of inorganic phosphate in the presence of labile organic phosphate and high concentrations of protein: application to lens ATPases. *Anal. Biochem.* **168**, 1–4 (1988).
35. Mastronarde, D. N. Automated electron microscope tomography using robust prediction of specimen movements. *J. Struct. Biol.* **152**, 36–51 (2005).
36. Biyani, N. et al. Focus: the interface between data collection and data processing in cryo-EM. *J. Struct. Biol.* **198**, 124–133 (2017).
37. Zheng, S. Q. et al. MotionCor2: anisotropic correction of beam-induced motion for improved cryo-electron microscopy. *Nat. Methods* **14**, 331–332 (2017).
38. Rohou, A. & Grigorieff, N. CTFFIND4: Fast and accurate defocus estimation from electron micrographs. *J. Struct. Biol.* **192**, 216–221 (2015).
39. Zhang, K. Gctf: real-time CTF determination and correction. *J. Struct. Biol.* **193**, 1–12 (2016).
40. Punjani, A., Rubinstein, J. L., Fleet, D. J. & Brubaker, M. A. cryoSPARC: algorithms for rapid unsupervised cryo-EM structure determination. *Nat. Methods* **14**, 290–296 (2017).
41. Kimanius, D., Forsberg, B. O., Scheres, S. H. & Lindahl, E. Accelerated cryo-EM structure determination with parallelisation using GPUs in RELION-2. *eLife* **5**, e18722 (2016).
42. Rosenthal, P. B. & Henderson, R. Optimal determination of particle orientation, absolute hand, and contrast loss in single-particle electron cryomicroscopy. *J. Mol. Biol.* **333**, 721–745 (2003).
43. Kucukelbir, A., Sigworth, F. J. & Tagare, H. D. Quantifying the local resolution of cryo-EM density maps. *Nat. Methods* **11**, 63–65 (2014).
44. Emsley, P., Lohkamp, B., Scott, W. G. & Cowtan, K. Features and development of Coot. *Acta Crystallogr. D* **66**, 486–501 (2010).
45. Moriarty, N. W., Grosse-Kunstleve, R. W. & Adams, P. D. Electronic ligand builder and optimization workbench (eLBOW): a tool for ligand coordinate and restraint generation. *Acta Crystallogr. D* **65**, 1074–1080 (2009).
46. Adams, P. D. et al. PHENIX: a comprehensive Python-based system for macromolecular structure solution. *Acta Crystallogr. D* **66**, 213–221 (2010).
47. Chen, V. B. et al. MolProbity: all-atom structure validation for macromolecular crystallography. *Acta Crystallogr. D* **66**, 12–21 (2010).

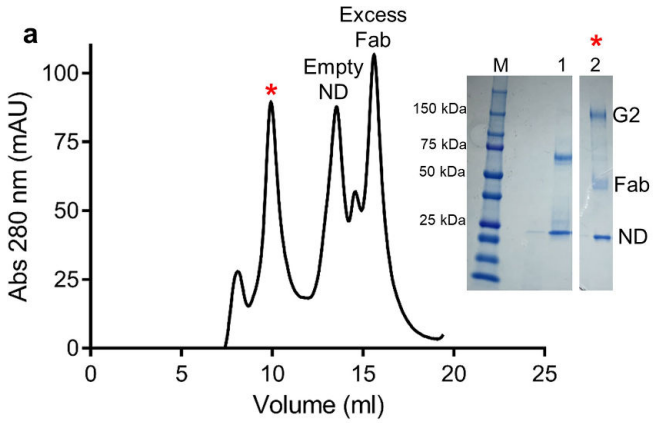

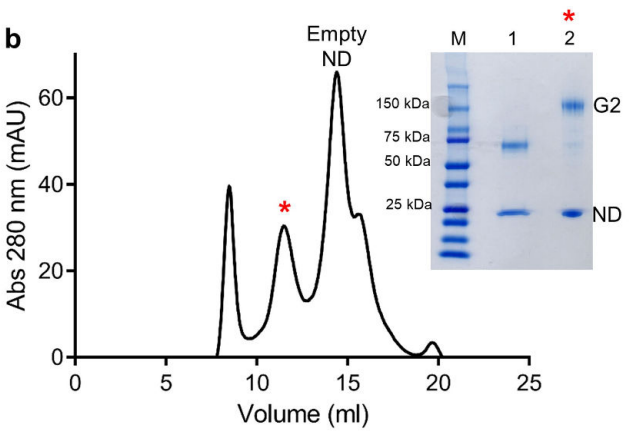

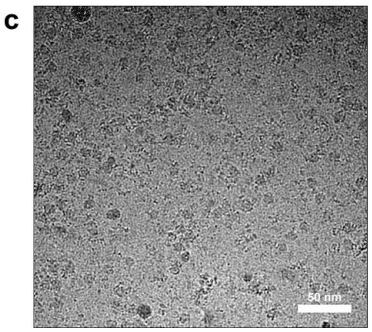

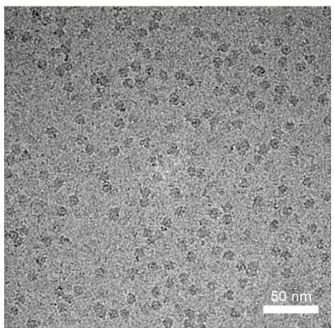

e

Sample	ATPase activity in nanodiscs (nmol min^{-1} mg^{-1})	Transport activity in proteoliposomes (nmol min^{-1} mg^{-1})
G2	768.4 ± 64.5 (n=7)	21.9 ± 3.4 (n=8)
E211Q	34.1 ± 6.4 (n=5)	1.7 ± 1.3 (n=8)

Extended Data Fig. 1 | Purification, activity and cryo-EM micrographs of ABCG2. a, Preparative SEC profile (milli absorbance units (mAU) at 280 nm plotted against retention volume (ml)) of the nanodisc-reconstituted $ABCG2_{EQ}$–E_1S complex. The fraction used for cryo-EM grid preparation is indicated by a red asterisk. Inset: reducing (lane 1) and non-reducing (lane 2) SDS–PAGE of the complex, showing bands for ABCG2 (G2), 5D3-Fab (Fab) and nanodisc (ND). **b**, Preparative SEC profile of the nanodisc-reconstituted $ABCG2_{EQ}$–ATP complex. The fraction used for cryo-EM grid preparation is indicated by a red asterisk. Inset: reducing (lane 1) and non-reducing (lane 2) SDS–PAGE of the complex, showing bands for ABCG2 (G2) and nanodisc (ND). **c**, An example micrograph (drift-corrected, dose-weighted and low-pass-filtered to 20 Å) of the nanodisc-reconstituted $ABCG2_{EQ}$–E_1S sample. White scale bar, 50 nm. **d**, An example micrograph (drift-corrected, dose-weighted and low-pass-filtered to 20 Å) of the nanodisc-reconstituted $ABCG2_{EQ}$–ATP sample. White scale bar, 50 nm. **e**, ATPase activities of nanodisc-reconstituted and E_1S-transport activities of liposome-reconstituted ABCG2. In both cases, data for wild-type and mutant (E211Q) ABCG2 are shown. The standard deviation from *n* technical replicates (same batch of nanodiscs or liposomes) is shown.

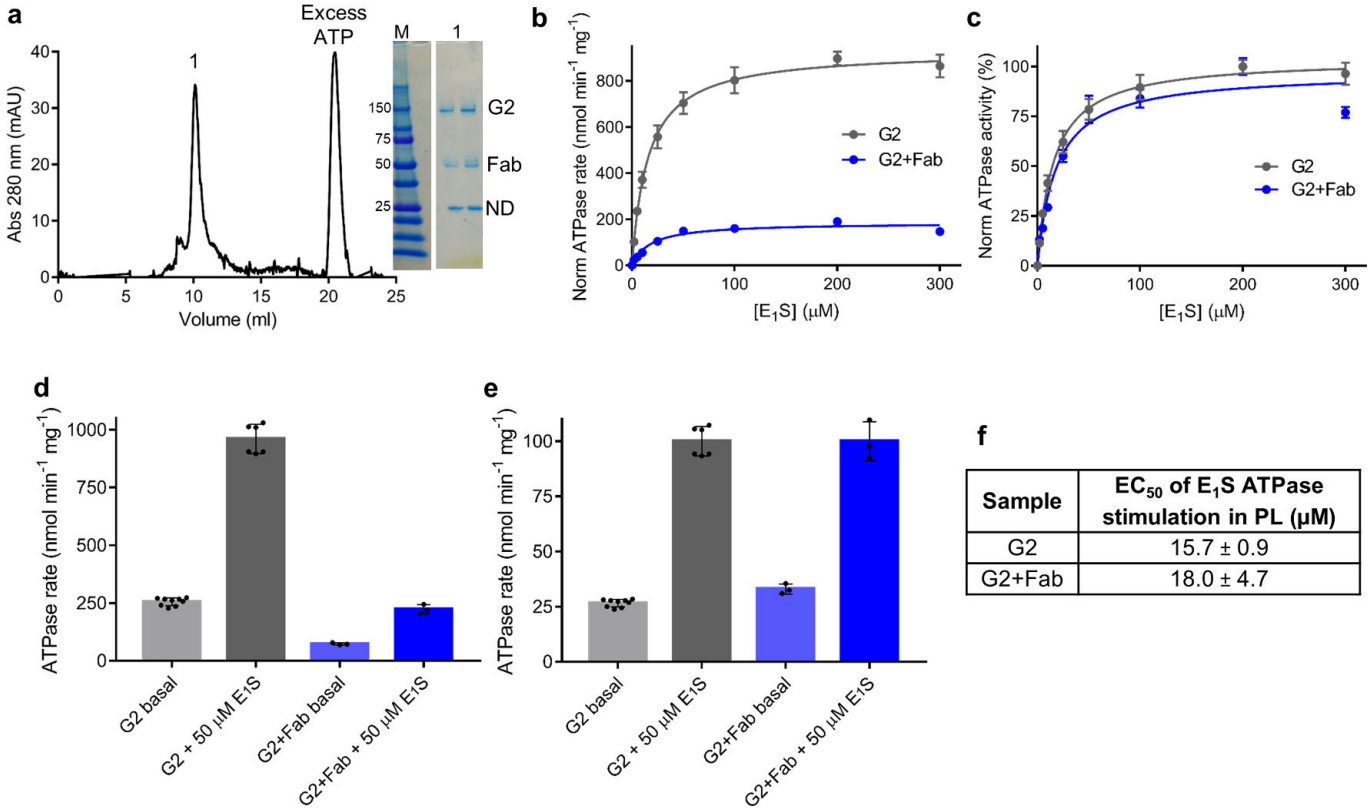

f

Sample	EC_{50} of E_1S ATPase stimulation in PL (μM)
G2	15.7 ± 0.9
G2+Fab	18.0 ± 4.7

Extended Data Fig. 2 | Effect of 5D3-Fab on ABCG2 function. **a**, Analytical SEC profile of the nanodisc-reconstituted $ABCG2_{EQ}$–E_1S complex in the presence of 5 mM ATP and 5 mM $MgCl_2$. '1' denotes the peak collected. Inset: non-reducing SDS–PAGE of the complex, showing bands for ABCG2 (G2), 5D3-Fab (Fab) and nanodisc (ND). **b**, ATPase activity of liposome-reconstituted ABCG2, in the presence or absence of 5D3-Fab, and with 0–300 μM E_1S. The basal ATPase activity has been normalized (norm) to 0. **c**, As for **b**, but with the maximal ATPase activity set to 100%. Each point represents the mean rate derived from technical replicates. For G2 $n = 6$, except in the case of 0 and 200 μM E_1S, for which $n = 9$. For G2 + Fab, $n = 3$. **d**, ATPase activities of ABCG2 in the presence and absence of 5D3-Fab, and either 0 or 50 μM E_1S. **e**, As for **d**, but with activities in the presence of E_1S set to 100%. Bars show means and dots show the rates derived from each technical replicate (same batch of liposomes). Error bars show the standard deviation. **f**, The EC_{50} of E_1S ATPase stimulation determined using the curves in **b** and **c** with the error of the fit (standard deviation) shown. PL, proteoliposome.

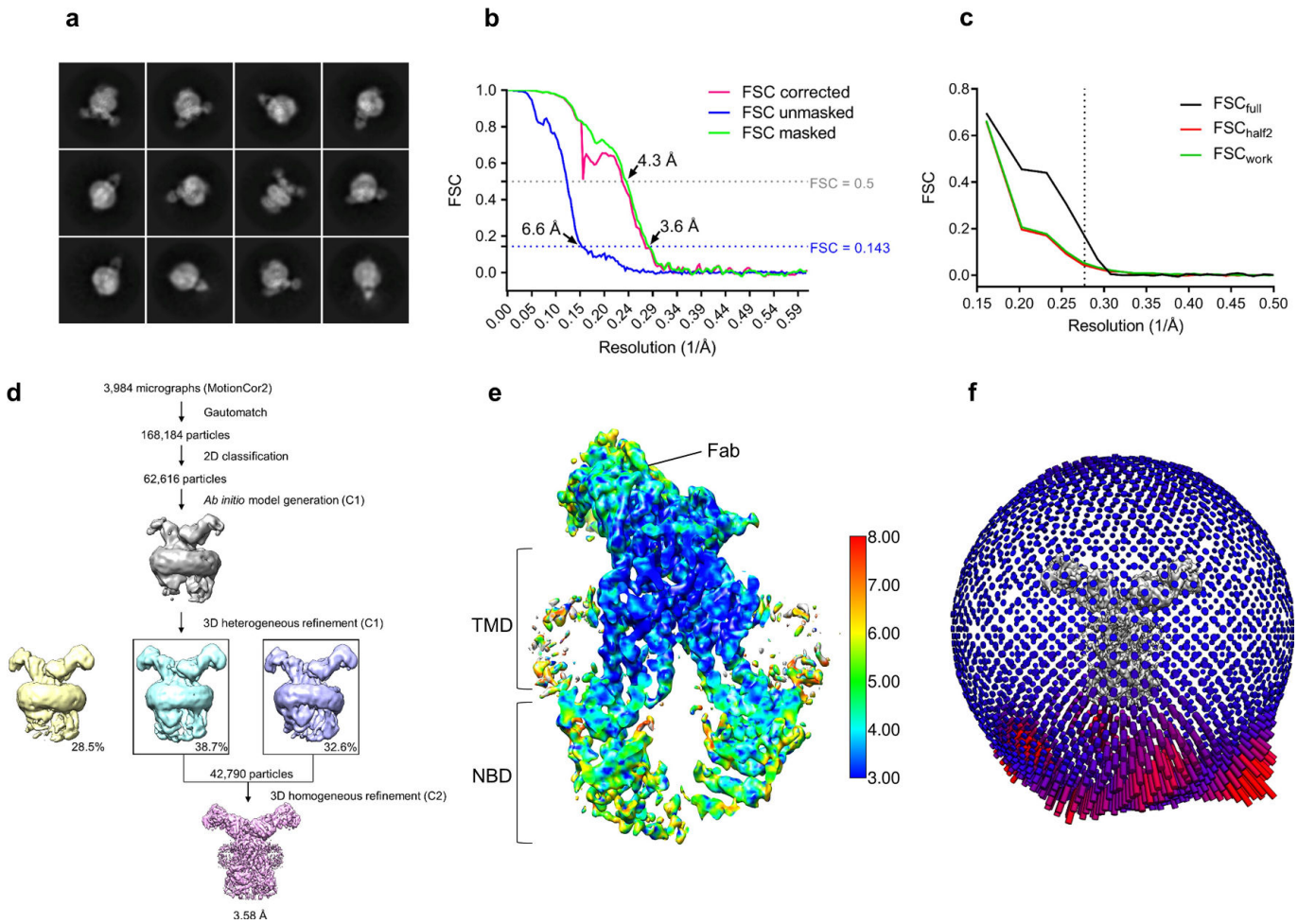

Extended Data Fig. 3 | Cryo-EM map generation, data processing and atomic-model refinement of ABCG2$_{EQ}$–E$_1$S. a, Twelve representative 2D class averages of the final round of 2D classification, sorted in decreasing order by the number of particles assigned to each class. **b**, FSC from the CryoSPARC auto-refine procedure of the unmasked half-maps (blue), the half-maps after masking (green), and the half-maps after masking and correction for the influence of the mask (pink). A horizontal dotted line (blue) is drawn for the FSC = 0.143 criterion. For both the unmasked and the corrected FSC curves, their intersection with the FSC = 0.143 and the FSC = 0.5 lines are marked by arrows, and the resolutions at these points are indicated. **c**, FSC curve of the final 3.58 Å refined model versus the map against it was refined (FSC$_{full}$; black line). The FSC curve of the final refined model with introduced shifts (mean value of 0.3 Å) versus the first of two independent half-maps (half-map 1, against which it was refined; FSC$_{work}$; green line) or the same model versus the second independent half-map (against which it was not refined; FSC$_{half2}$; red line) is also shown. **d**, Flow chart for cryo-EM data processing and structure determination of the ABCG2$_{EQ}$–E$_1$S complex. **e**, Full view of the final CryoSPARC B-factor-sharpened map of ABCG2$_{EQ}$–E$_1$S, coloured by local resolution in Å, as calculated by ResMap with the clipping plane in the middle of the molecule. **f**, Angular distribution plot for the final reconstruction.

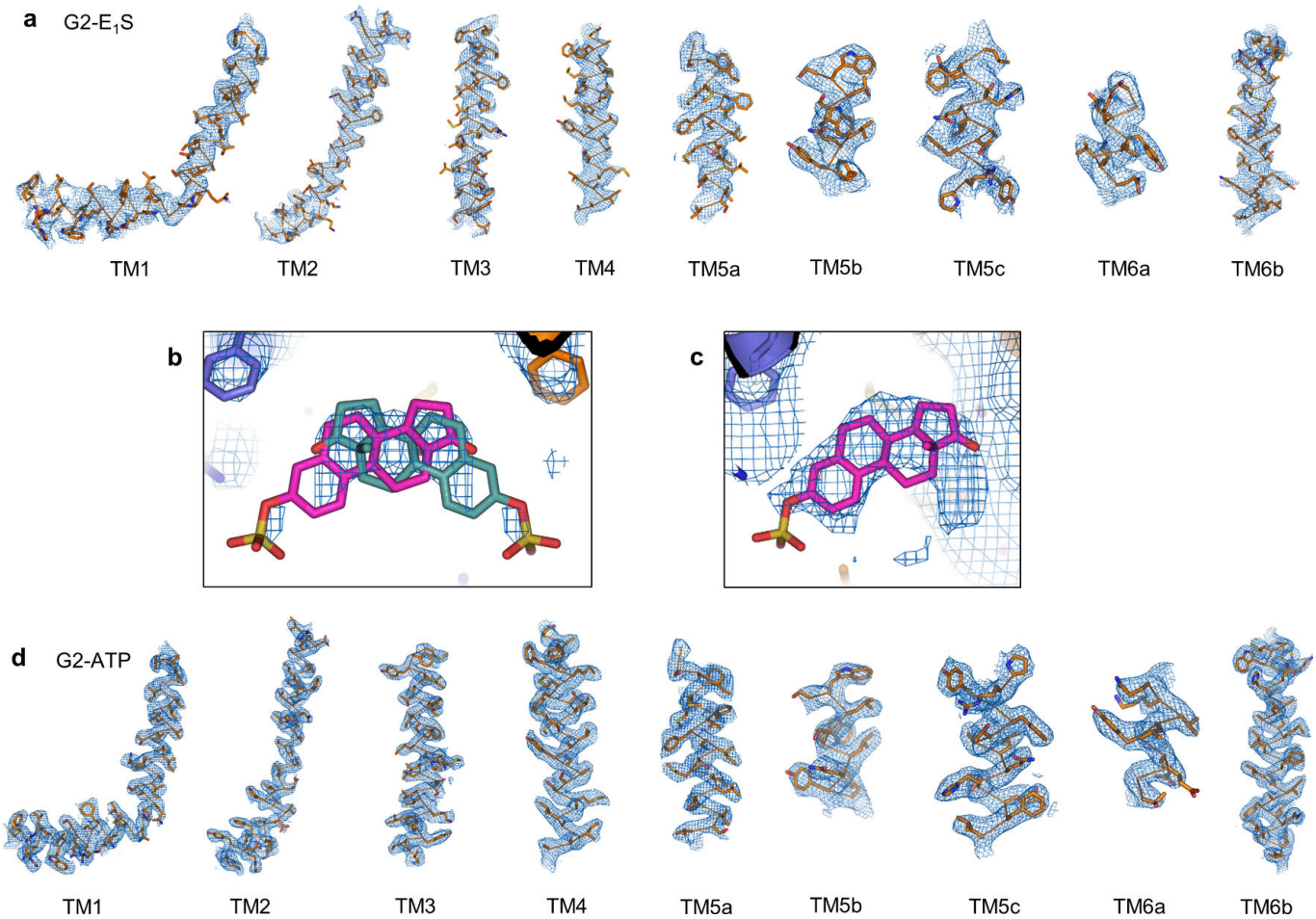

Extended Data Fig. 4 | Fit of the models to the densities. a, Fit of the TM helices of the final model of the $ABCG2_{EQ}$–E_1S TMD to the post-processed and masked C2 map from CryoSPARC. A region of up to 2 Å around the atoms is shown. **b**, The fit of one E_1S molecule (pink or turquoise sticks) in two possible orientations, flipped by 180°, docked into the C2-symmetrized substrate density of the final model of $ABCG2_{EQ}$–E_1S. The contour level has been reduced by comparison with Fig. 2a to show the strongest density at the core of the polycyclic rings. **c**, As for **b**, but showing the fit of one E_1S into the electron microscopy density of the post-processed and masked C1 map from CryoSPARC. **d**, Fit of the TM helices of the final model of the $ABCG2_{EQ}$–ATP TMD to the post-processed and masked C2 map from RELION. A region of up to 2 Å around the atoms is shown.

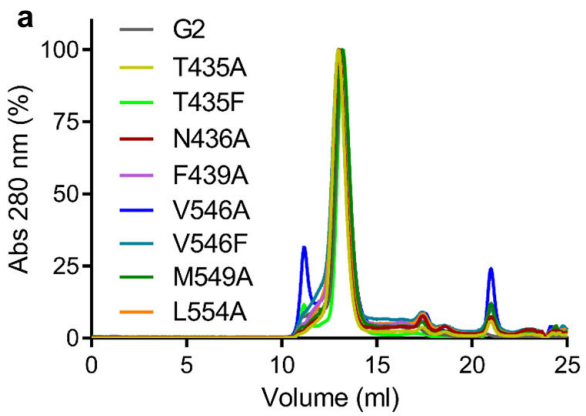

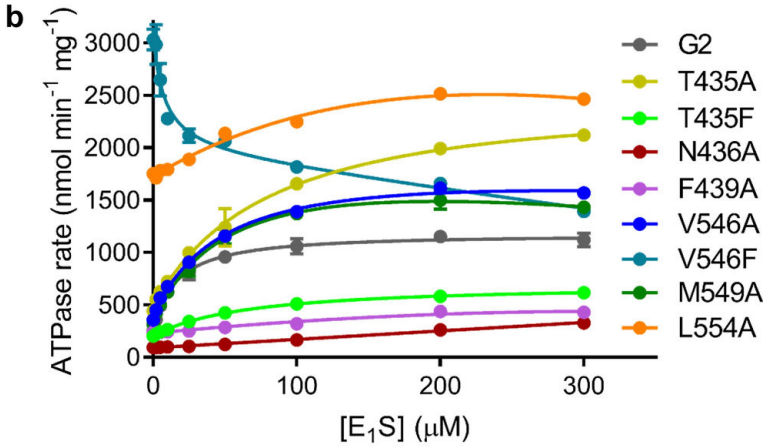

c

Sample	EC_{50} of E_1S ATPase stimulation in PL (μM)
G2	15.7 ± 0.9
T435A	71.7 ± 6.0
T435F	66.5 ± 1.9
N436A	Not determined
F439A	Not determined
V546A	36.3 ± 3.4
V546F	Inhibition by E_1S
M549A	31.3 ± 4.1
L554A	108.0 ± 33.5

Extended Data Fig. 5 | Purification and functional analysis of mutants. **a**, Analytical SEC profiles of the detergent-purified wild-type and substrate-binding cavity mutants used to make proteoliposomes for functional assays. **b**, ATPase rates of the liposome-reconstituted wild-type and mutant proteins in the presence of 0–300 μM E_1S. Each point represents the mean rate derived from technical replicates (same batch of liposomes) and error bars show the standard deviation. For G2, $n = 6$, except in the case of 0 and 200 μM E_1S, for which $n = 9$. For the mutants, $n = 3$. **c**, Table showing the EC_{50} of E_1S ATPase stimulation determined after normalizing the curves in **b** with the error of the fit (standard deviation) shown.

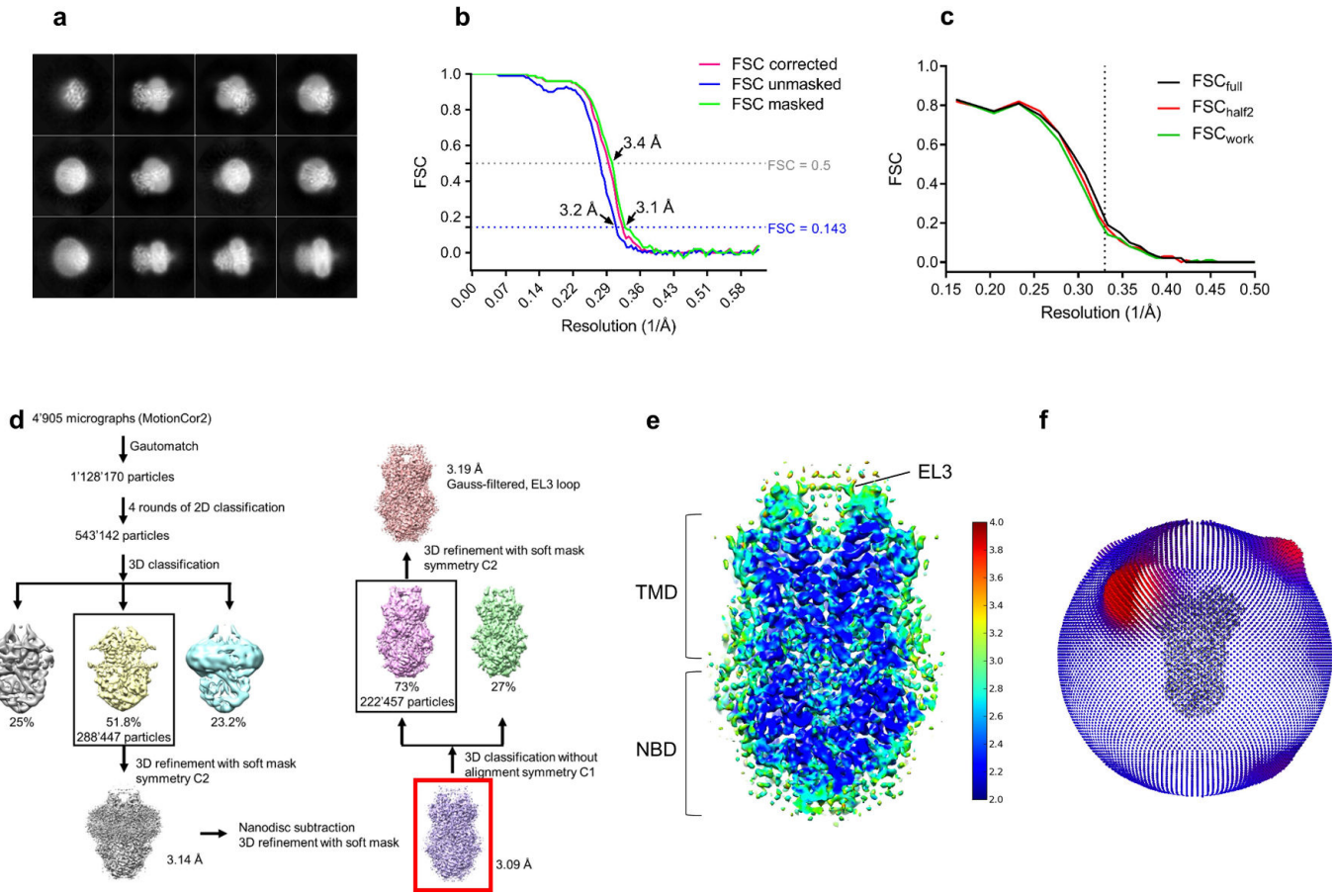

Extended Data Fig. 6 | Cryo-EM map generation, data processing and atomic-model refinement of ABCG2$_{EQ}$–ATP. a, Twelve representative 2D class averages of the final round of 2D classification, sorted in decreasing order by the number of particles assigned to each class. **b**, FSC from the RELION auto-refine procedure of the unmasked half-maps (blue), the half-maps after masking (green), and the half-maps after masking and correction for the influence of the mask (pink). A horizontal dotted line (blue) is drawn for the FSC = 0.143 criterion. For both the unmasked and the corrected FSC curves, their intersection with the FSC = 0.143 and the FSC = 0.5 lines are marked by arrows, and the resolutions at these points are indicated. **c**, FSC curve of the final 3.09 Å refined model versus the map against which it was refined (FSC$_{full}$; black line). FSC curves of the final refined model with introduced shifts (mean value of 0.3 Å) versus the first of two independent half-maps (half-map 1, against which it was refined; FSC$_{work}$; green line) or the same model versus the second independent half-map (against which it was not refined; FSC$_{half2}$; red line) are also shown. **d**, Flow chart for cryo-EM data processing and structure determination of the ABCG2$_{EQ}$–ATP complex. The map used for model building is indicated by a red square. **e**, Full view of the RELION local-resolution-filtered map of ABCG2$_{EQ}$–ATP, coloured by local resolution in Å as calculated by ResMap, with the clipping plane in the middle of the molecule. **f**, Angular distribution plot for the final reconstruction.

Extended Data Table 1 | Cryo-EM data collection, refinement and validation statistics

	$ABCG2_{EQ}$-E_1S (EMD-0196, PDB 6HCO)	$ABCG2_{EQ}$-ATP (EMD-0190, PDB 6HBU)
Data collection and processing		
Magnification (nominal)	61,610× (165k×)	61,610× (165k×)
Voltage (kV)	300	300
Electron exposure (e–/Å^2)	2.0	2.0
Defocus range (μm)	-0.7 to -2.8	-0.5 to -3.3
Pixel size (Å)	0.812	0.812
Symmetry imposed	C2	C2
Initial particle images (no.)	168,184	1,128,170
Final particle images (no.)	42,790	288,447
Map resolution (Å)	3.58	3.09
FSC threshold	0.143	0.143
Map resolution range (Å)	308.6-3.58	308.6-3.09
Refinement		
Initial model used	PDB 6ETI	PDB 6ETI
Model resolution (Å)	3.58	3.09
FSC threshold	0.143	0.143
Model resolution range (Å)	207.0-3.6	207.0-3.1
Map sharpening *B* factor (Å^2)	-82.6	-136.0
Model composition		
Nonhydrogen atoms	12,338	9,144
Protein residues	1576	1168
Ligands	24	64
B factors (Å^2)		
Protein	140.93	22.25
Ligand	118.32 (E_1S)	9.3 (ATP) 4.1 (Mg^{2+})
R.m.s. deviations		
Bond lengths (Å)	0.009	0.009
Bond angles (°)	1.010	1.087
Validation		
MolProbity score	1.82	1.61
Clashscore	7.26	4.34
Poor rotamers (%)	0.45	0.00
Ramachandran plot		
Favored (%)	92.20	94.62
Allowed (%)	7.80	5.03
Disallowed (%)	0.00	0.35

For the $ABCG2_{EQ}$–E_1S structure, only the variable domain of 5D3-Fab was modelled.

nature research

Corresponding author(s): Kaspar P Locher

Reporting Summary

Nature Research wishes to improve the reproducibility of the work that we publish. This form provides structure for consistency and transparency in reporting. For further information on Nature Research policies, see Authors & Referees and the Editorial Policy Checklist.

Statistical parameters

When statistical analyses are reported, confirm that the following items are present in the relevant location (e.g. figure legend, table legend, main text, or Methods section).

n/a	Confirmed	
☐	☒	The exact sample size (*n*) for each experimental group/condition, given as a discrete number and unit of measurement
☐	☒	An indication of whether measurements were taken from distinct samples or whether the same sample was measured repeatedly
☒	☐	The statistical test(s) used AND whether they are one- or two-sided *Only common tests should be described solely by name; describe more complex techniques in the Methods section.*
☒	☐	A description of all covariates tested
☒	☐	A description of any assumptions or corrections, such as tests of normality and adjustment for multiple comparisons
☐	☒	A full description of the statistics including central tendency (e.g. means) or other basic estimates (e.g. regression coefficient) AND variation (e.g. standard deviation) or associated estimates of uncertainty (e.g. confidence intervals)
☒	☐	For null hypothesis testing, the test statistic (e.g. *F*, *t*, *r*) with confidence intervals, effect sizes, degrees of freedom and *P* value noted *Give P values as exact values whenever suitable.*
☒	☐	For Bayesian analysis, information on the choice of priors and Markov chain Monte Carlo settings
☒	☐	For hierarchical and complex designs, identification of the appropriate level for tests and full reporting of outcomes
☒	☐	Estimates of effect sizes (e.g. Cohen's *d*, Pearson's *r*), indicating how they were calculated
☐	☒	Clearly defined error bars *State explicitly what error bars represent (e.g. SD, SE, CI)*

Our web collection on statistics for biologists may be useful.

Software and code

Policy information about availability of computer code

Data collection	SerialEM 3.6.0
Data analysis	GraphPad Prism 7.00, Pymol 1.3, PHENIX 1.13-2998, Coot 0.8.9, RELION 2.0, MotionCor2, Gctf 1.06, Gautomatch 0.56, Chimera 1.10.2, CryoSPARC.

For manuscripts utilizing custom algorithms or software that are central to the research but not yet described in published literature, software must be made available to editors/reviewers upon request. We strongly encourage code deposition in a community repository (e.g. GitHub). See the Nature Research guidelines for submitting code & software for further information.

Data

Policy information about availability of data

All manuscripts must include a data availability statement. This statement should provide the following information, where applicable:

- Accession codes, unique identifiers, or web links for publicly available datasets
- A list of figures that have associated raw data
- A description of any restrictions on data availability

Atomic coordinates for ABCG2-E1S (5D3-Fab variable domain only), and ABCG2-ATP were deposited in the Protein Data Bank under accession codes 6HCO and 6HBU respectively. EM data for the two structures were deposited in the Electron Microscopy Data Bank under accession codes EMD-0196 (ABCG2-E1S) and

EMD-0190 (ABCG2-ATP). Source data for Figures 2e, f, Extended Data Figures 1e, 2b, d, f and 5 are available online. All other data are available from the corresponding author upon reasonable request. A Life Sciences Reporting Summary for this article is available.

Field-specific reporting

Please select the best fit for your research. If you are not sure, read the appropriate sections before making your selection.

☒ Life sciences ☐ Behavioural & social sciences ☐ Ecological, evolutionary & environmental sciences

For a reference copy of the document with all sections, see nature.com/authors/policies/ReportingSummary-flat.pdf

Life sciences study design

All studies must disclose on these points even when the disclosure is negative.

Sample size	No statistical methods were used to predetermine sample size. For the ATPase assays (Figure 2e, Extended Data Figures 1e, 2b-f and 5) at least three technical replicates (same batch of liposomes or nanodiscs) were completed with four time points recorded for each replicate. For the transport assays (Figure 2f) at least four technical replicates were completed. For all bar graphs (Figures 2e,f and Extended Data Figure 2d,e) the mean rate for each technical replicate has been plotted. Source Data has been provided.
Data exclusions	No data excluded
Replication	All replicates were successful. The experimental conditions described in the Methods and/or referenced were adhered to as strictly as possible.
Randomization	Animals and humans were not used in the study. Randomisation was not applicable as we used predetermined samples, conditions and time points in our assays.
Blinding	Animals and humans were not used in the study. Blinding was not applicable as we used predetermined samples, conditions and time points in our assays.

Reporting for specific materials, systems and methods

Materials & experimental systems

n/a	Involved in the study
☒	☐ Unique biological materials
☐	☒ Antibodies
☐	☒ Eukaryotic cell lines
☒	☐ Palaeontology
☒	☐ Animals and other organisms
☒	☐ Human research participants

Methods

n/a	Involved in the study
☒	☐ ChIP-seq
☒	☐ Flow cytometry
☒	☐ MRI-based neuroimaging

Antibodies

Antibodies used	The 5D3-antibody (reference 15 in the manuscript) was provided by B.Sorrentino whom we thank in the acknowledgments.
Validation	The 5D3-antibody was generated specifically for ABCG2 and has been biochemically validated (references 13 and 14 in the manuscript).

Eukaryotic cell lines

Policy information about cell lines

Cell line source(s)	HEK293 EBNA (Thermo Fisher Scientific).
Authentication	No
Mycoplasma contamination	No

Commonly misidentified lines (See ICLAC register)	N/A